ELSEVIER

Catalysis Today 79–80 (2003) 203–210

CATALYSIS TODAY

www.elsevier.com/locate/cattod

# MRI visualisation of two-phase flow in structured supports and trickle-bed reactors

L.F. Gladden [a,*], M.H.M. Lim [a], M.D. Mantle [a], A.J. Sederman [a], E.H. Stitt [b]

[a] *Department of Chemical Engineering, University of Cambridge, Pembroke Street, Cambridge CB2 3RA, UK*
[b] *Synetix, P.O. Box 1, Billingham TS23 1LB, Cleveland, UK*

**Abstract**

We demonstrate the application of magnetic resonance imaging (MRI) to provide quantitative visualisation of two-phase flow in two different reactor environments. First, visualisation and analysis of bubble-train flow within individual channels in a ceramic monolith are presented. Images are acquired over time-scales of 146 ms, thereby enabling the movement of individual gas bubbles to be followed in real time. From these data, distributions of bubble size and velocity are obtained. Second, MRI is used to obtain measurements of liquid hold-up and wetting efficiency during co-current air–water trickle flow in fixed beds of packings of cylindrical, porous alumina extrudate. Data are reported for a constant gas superficial velocity of 31.3 mm/s, and liquid superficial velocities in the range 0.1–6 mm/s. The dynamic liquid hold-up data are well modelled using the percolation analysis of Crine et al. [Chem. Eng. Sci. 47 (1992) 2263].


*Keywords:* Magnetic resonance imaging; Bubble-train flow; Trickle-bed reactor; Two-phase flow

## 1. Introduction

Over the past 10 years there has been increasing interest in the application of tomographic methods to the study of catalytic reactors. Examples of such studies include the use of conductance and capacitance methods [2], optical methods [3], and X-ray tomography [4]. In recent years there has been increasing interest in applying magnetic resonance imaging and transport measurement techniques to study various aspects of chemical and biochemical reactor operation [5–13]. The purpose of this paper is to highlight the state-of-the-art capabilities of magnetic resonance imaging (MRI) in application to reaction engineering. A detailed description of the theoretical principles of magnetic resonance techniques is not included. For a rigorous treatment of the underlying physics the reader is directed to the text of Callaghan [14]; a review of the general principles of magnetic resonance along with examples of how the method allows us to probe systems of interest to chemical engineers may also be useful [15].

This paper considers the application of MRI to quantify two-phase flow in two different reactor environments. Both examples highlight the capability of MRI to visualise the distribution of gas and liquid within optically opaque, magnetically heterogeneous systems. First, we consider bubble-train flow in a ceramic monolith. The motivation for this study is to gain a better understanding of two-phase flow in straight-channel structured supports with regard to potential applications in the fine chemicals industries. In contrast to their applications in gas phase catalysis, application of monoliths to gas–liquid reactions is not

* Corresponding author. Tel.: +44-1223-334762; fax: +44-1223-334796.
*E-mail address:* gladden@cheng.cam.ac.uk (L.F. Gladden).

0920-5861/03/$ – see front matter 
doi:10.1016/S0920-5861(03)00006-3

well advanced due to the lack of understanding of the heat and mass transfer processes occurring [16]. Application of MRI to study flow and reaction in monoliths has also recently been addressed by Koptyug et al. [17] and Heibel et al. [18]. The former work reported thermally polarised $^{1}$H NMR microimaging studies of single phase gas flow in monolithic catalysts for which typical image acquisition times were 20–40 min. Heibel et al. [18] reported investigations of gas and liquid distributions in the plane perpendicular to the direction of superficial flow in the film flow regime and, in particular, addressed the accumulation of liquid in the corners of the square channels of the monolith. The work reported in this paper focuses on applying fast visualisation techniques such that the dynamics of the gas and liquid flow within individual channels can be followed. We also report MRI visualisation and quantitative analysis of trickle flow in a packed bed of porous alumina catalyst support. In earlier work [8] we have shown that MRI can be used to measure liquid hold-up and wetting efficiency in packed beds of non-porous glass ballotini. Here we show that the same information can be obtained for porous packings, by exploiting relaxation contrast to differentiate between liquid in the inter- and intra-particle space in the bed.

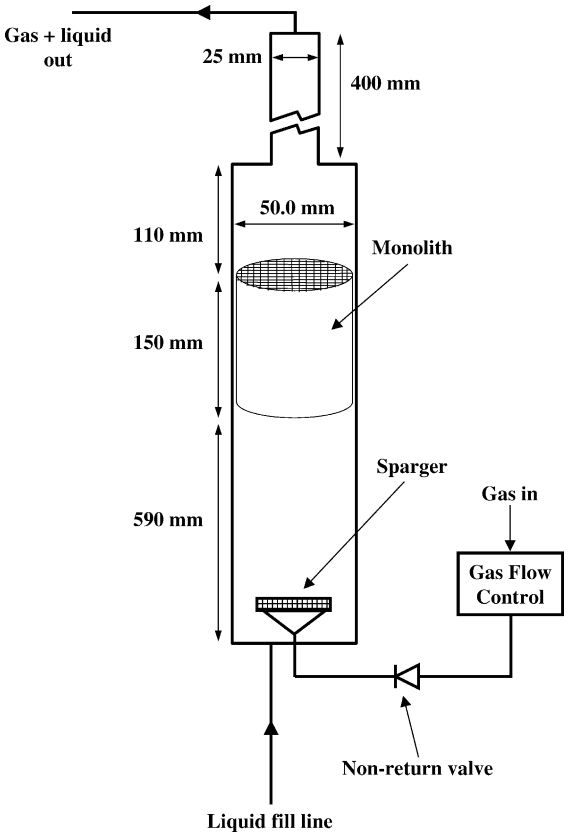


Fig. 1. Schematic of the experimental set-up for the imaging studies of two-phase flow through a ceramic monolith.

## 2. Experimental and data analysis

All magnetic resonance visualisations were performed on a Bruker Spectrospin DMX 200, 4.7 T magnet with a birdcage coil of length and diameter 6.3 cm. $^{1}$H images were acquired at a frequency of 199.7 MHz. Spatial resolution was achieved using shielded gradient coils providing a maximum gradient strength of 13.90 G/cm.

### 2.1. Two-phase flow in a ceramic monolith

The experimental apparatus consists of a vertical column containing a ceramic (cordierite) monolith, rated at 300 channels per square inch. A schematic of the experimental set-up is given in Fig. 1. The inner diameter and total length of the column were 50 mm and 1.25 m, respectively. The monolith was of length 150 mm, and the bottom face of the monolith was positioned 590 mm from the inlet to the column. The centre of the imaging volume was aligned with the centre of the monolith. The monolith was initially flooded with a 0.5 v/v % solution of propan-2-ol in water to a height 500 mm above the top face of the monolith. The data presented are for the case of gas up-flow through stagnant liquid. The gas (compressed air) was introduced into the liquid at the bottom of the column through a sparger. Gas was introduced at flow rates of 100, 150, 200 and 300 ml/min.

The pulse sequence used is based on the 2D ‘Single Shot RARE’ (or Turbo Spin Echo) pulse sequence [19]. In the present modification the pulse sequence is modified such that four images are acquired in immediate succession, each image having a data acquisition time of 146 ms [20,21]. Effective image times are taken as 74, 220, 366 and 512 ms after the initial excitation. Subsequent sets of four images were acquired

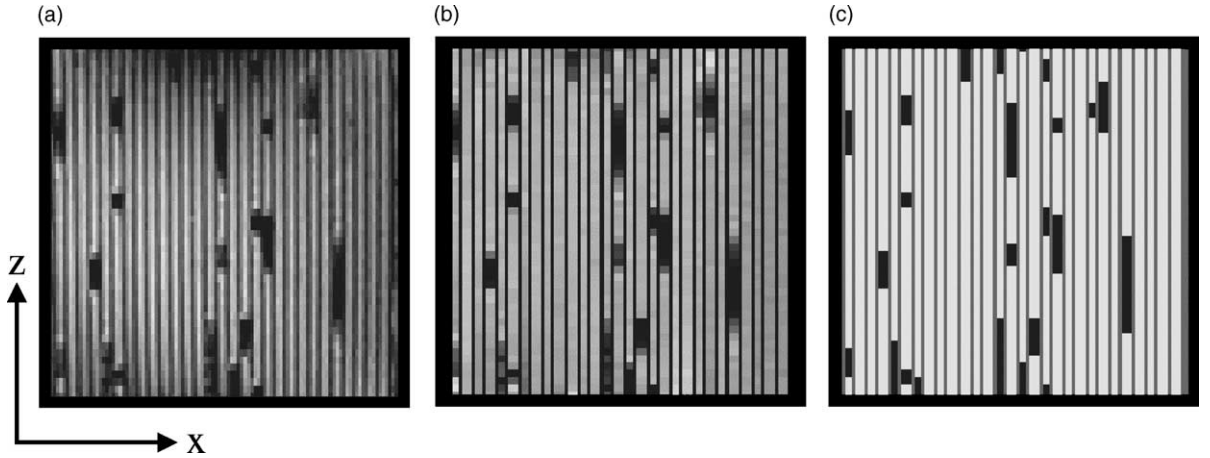


Fig. 2. (a) Single *XZ* image acquired of gas–liquid distribution within a ceramic monolith. Data are shown for a gas flow rate of 100 ml/min. In-plane spatial resolution is 395 μm (*X*) × 791 μm (*Z*); bubble motion is along the length of the channels, in the *Z*-direction. No signal is obtained from the gas, hence gas bubbles within the channels are identified as regions of zero signal intensity (dark shades) in the image. (b) The map produced from the image shown in (a) following correction to the image intensities arising from r.f. inhomogeneity, and averaging of the signal intensities across the width of each channel. (c) The ternary-gated map derived from (a) and (b), identifying gas (black), solid (grey) and liquid (white).

following a time delay of 20 s over a total sampling period of approximately 40 min. The field-of-view in the *XZ* plane was 5.06 cm × 5.06 cm yielding an in-plane spatial resolution of 395 μm × 791 μm for a data matrix size of 128 × 64. The thickness of the image slice is 0.6 mm.

Fig. 2a shows typical data recorded; the location of gas bubbles within individual channels of the monolith are clearly identified. From such data, measurement of phase distribution and bubble size (length) are obtained. The velocity with which a bubble is moving within a channel is determined by identifying the position of a given gas–liquid interface between successive images of gas–liquid distribution.

To obtain meaningful statistics from the MRI data, we have developed robust image analysis techniques which provide an automated analysis of the images such that the reported bubble size distributions are based on 1000–2000 bubbles and velocity distributions are based on bubbles in, typically, 500 channels. The key step in the image analysis is an accurate identification of the gas–liquid interface. This is achieved by binary gating the acquired image at a value at the mid-point in the distribution of signal intensities within the image. Maximum signal intensity is associated with liquid-filled pixels, and minimum signal intensity is associated with gas-filled pixels [21]. To obtain a robust identification of the position of the gas–liquid interface two procedures are introduced: (i) To overcome the effects of radio frequency (r.f.) inhomogeneity, which gives rise to the decrease in overall signal intensity at the lower and upper regions of the image (see Fig. 2a), the signal intensity associated with each pixel is normalised to the locally averaged signal intensity. This procedure produces an image in which all pixels which are completely filled with water have approximately the same signal intensity. (ii) The image intensity across a single channel is averaged (the width of each channel corresponds to approximately three pixels) to overcome decreases in signal intensity, arising from partially liquid-filled pixels associated with pixels at the monolith-liquid interface. This analysis is implemented to provide a robust (i.e. reproducible) measure of the average position of the gas–liquid interface; curvature effects of that interface are ignored since they are below the level of spatial resolution of the experiment. Bubble lengths obtained from this analysis are accurate to ±395 μm. Fig. 2b shows the image shown in Fig. 2a, following implementation of these two steps in the data analysis. Having recorded a visualisation of a fully liquid-saturated monolith to identify the channels directly, and following the

identification of gas–liquid interfaces, a map is derived from the image in which three phases are identified: solid (monolith), liquid and gas (Fig. 2c). The length of a given bubble is determined directly from Fig. 2c. The velocity with which a given bubble moves within a channel is calculated by identifying the distance moved by a given gas–liquid interface between two successive images acquired from a single excitation. Where several bubbles were observed within the same channel, the average velocity of the bubbles is taken.

### 2.2. Two-phase flow in a trickle-bed reactor

Air–water trickle flow is studied through fixed beds of randomly packed cylindrical, porous alumina extrudate. Details of the experimental procedures are reported elsewhere [8]. Data for two packings are reported: (i) packing of diameter 1.5 mm and a distribution of lengths in the range $5 \pm 2$ mm; (ii) packing of diameter and length equal to 3 mm. The packings were loaded into a cylindrical column of length and inner diameter 500 and 40 mm, respectively. The porosity of the beds packed with 1.5 and 3 mm packings were $0.41 \pm 0.02$ and $0.30 \pm 0.02$, as determined by MRI, and $0.38 \pm 0.03$ and $0.29 \pm 0.03$ as determined by gravimetric water displacement. The beds were operated under co-current, down-flow in the trickle flow regime. Prior to introducing the gas–liquid flow the bed was fully wetted. Gas (compressed air) was introduced to the column at 2 bar. All data are shown for a constant gas superficial velocity of 31.3 mm/s. MRI visualisations of gas–liquid distribution through transverse sections of the bed, perpendicular to the direction of superficial flow, were then recorded for different values of the liquid superficial velocity through the bed. For each value of the liquid superficial velocity values of liquid hold-up ($\chi$) and wetting efficiency ($\chi_s$), as defined below, were determined [8]:

- $\chi$: The fraction of (inter-particle) void space pixels containing some liquid provides an upper estimate [8] of liquid saturation, from which values of liquid hold-up are obtained. By extrapolation of the data to zero liquid superficial velocity, the static liquid hold-up is identified, and hence the dynamic liquid hold-up, $\chi_{dynamic}$, is obtained.
- $\chi_s$: The wetting efficiency is obtained by calculating the fraction of the pixels identifying the surface of the packing, which contain liquid. Liquid-containing voxels adjacent to the wall of the column,

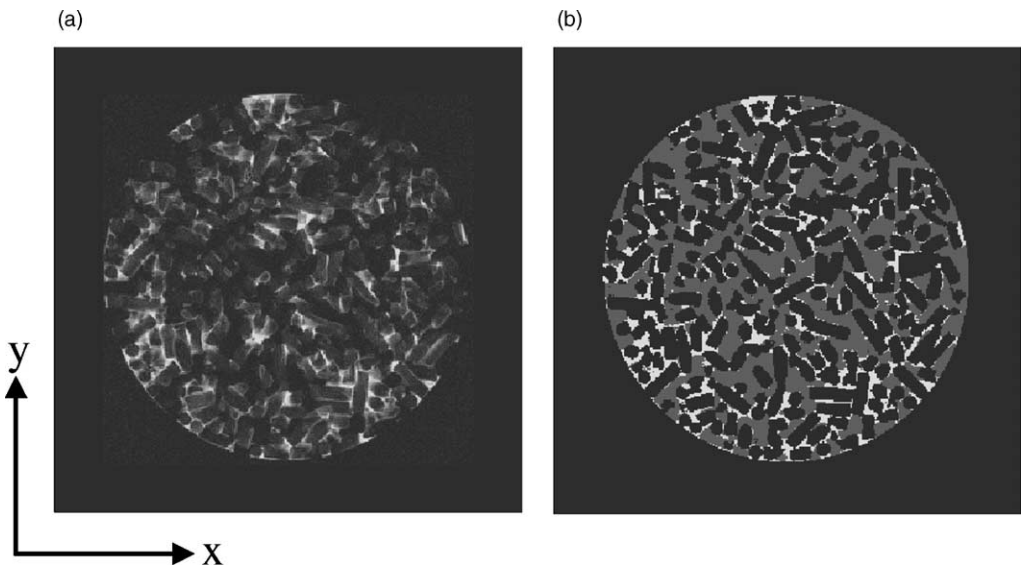


Fig. 3. (a) MRI image of air–water distribution during trickle flow. The gas and liquid superficial velocities are 31.3 and 0.5 mm/s, respectively. In-plane pixel resolution is 156 μm × 156 μm. (b) The ternary-gated map derived from the image shown in (a); solid-phase (black), liquid (white) and gas (grey).

as well as the internal surface of the porous packing elements are not considered in the analysis.

Two-dimensional (2D) visualisations of gas–liquid distribution within transverse sections, of thickness 1 mm, through the bed were acquired using a standard spin-warp imaging sequence. An echo time of 5 ms was employed such that signal from even the fastest flowing liquid within the bed was obtained. The total data acquisition time for each image is 25 min. Data were recorded with a field-of-view of 40 mm × 40 mm and a data array size of 256 × 256, thereby yielding an in-plane spatial resolution of 156 μm × 156 μm.

Whilst discrimination between gas and liquid within the image is straightforward since no signal is obtained from molecules in the gas phase, discrimination between liquid in the inter- and intra-particle space is less straightforward. Unambiguous determination of the position of the packing elements is achieved by multiplying any given image obtained under trickle flow conditions by a reference image of the same image slice, acquired under conditions in which only inter-particle liquid is visualised. Given typical spin-spin relaxation time values of water in the intra- and inter-particle space of 1.5 ms and 1.5 s, respectively, identification of the position of the packing within the bed was obtained using a RARE sequence [19] with a RARE factor of 64 resulting in an echo time of 172 ms. Fig. 3 shows a typical image and the ternary-gated map derived from this image identifying gas, liquid and solid-phases.

## 3. Results and discussion

### 3.1. Two-phase flow in a ceramic monolith

Fig. 4a shows the fraction of the total number of bubbles characterised by a given size (length). Data are shown for gas flow rates of 100, 150, 200 and 300 ml/min. Fig. 4b extends the distribution to larger bubble lengths. It is seen that at the higher liquid flow rates used, bubbles of length 18–20 mm exist. At the lowest flow rate studied (100 ml/min), few, if any, bubbles of length >10 mm exist. Fig. 5a shows the fraction of the total number of bubbles associated with a given bubble velocity within the monolith. Increasing gas flow is seen to give rise to a reduction in the population of bubbles associated with low velocities (0–10 mm/s) and a significant increase in the population of bubbles moving with high velocities (>30 mm/s). As gas flow rate increases from 100 to 300 ml/min, a transition in the bubble velocity distribution from an asymmetric unimodal distribution to a clearly resolved bimodal

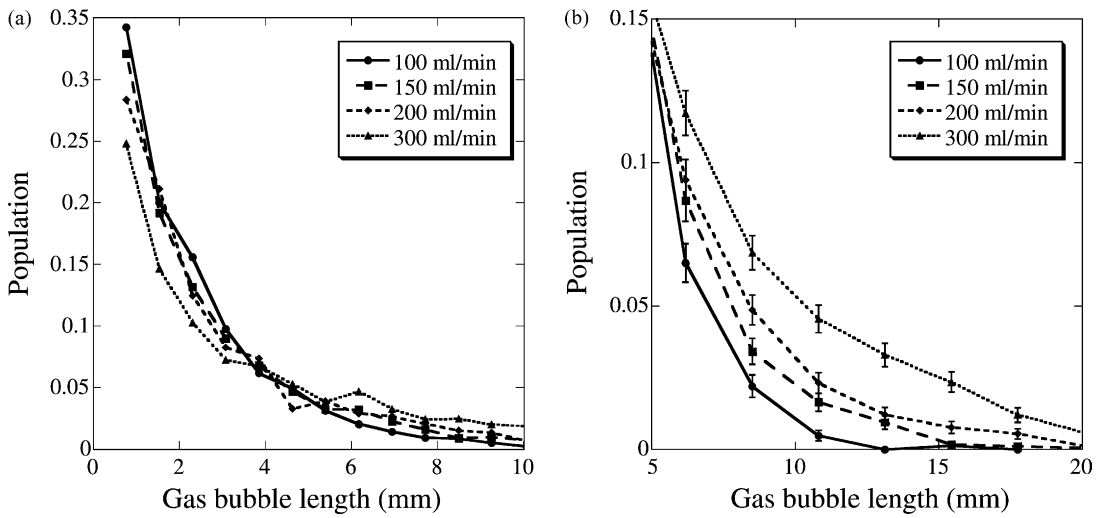


Fig. 4. (a) Fractional population of bubble lengths for each of the gas flow rates studied; the distribution is calculated with a bin size of 0.77 mm. (b) Bubble-length distributions for the same data as in (a), highlighting the population of bubbles of longer lengths; the bin size has been increased to 2.31 mm to improve signal-to-noise. The error bars represent the sampling errors of the distribution function.

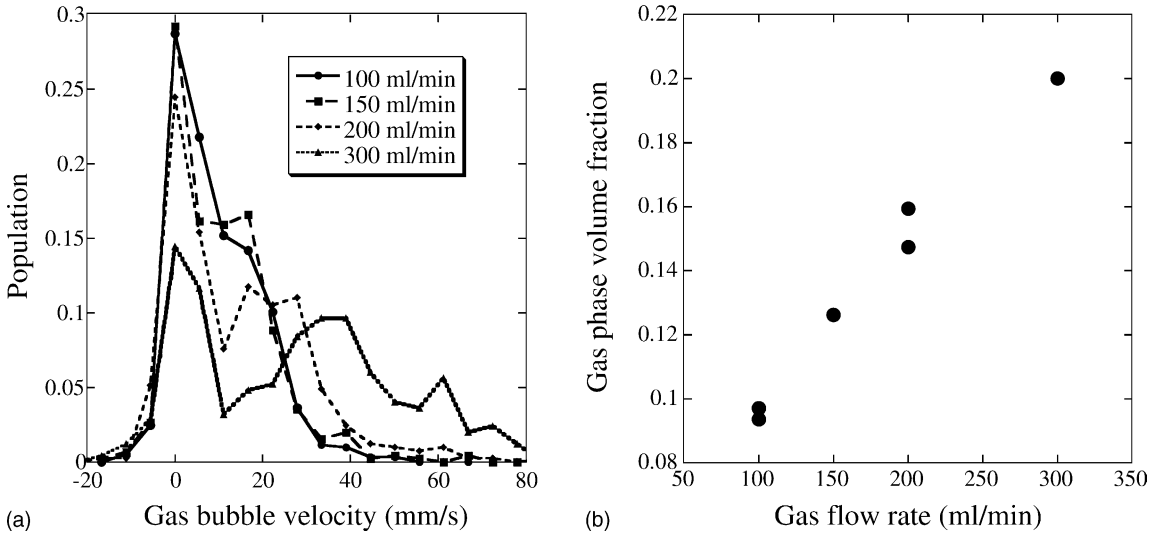


Fig. 5. (a) Fractional population of bubbles of a given velocity within the monolith, for each of the gas flow rates studied. (b) Gas phase volume fraction as a function of gas flow rate. For gas flow rates of 100 and 200 ml/min, the results of reproducibility experiments are also shown.

distribution is observed. For all gas flow rates studied, a small population of bubbles moving counter-current to the direction of superficial flow is also observed; such bubble motion was not observed to occur preferentially in either the peripheral or inner core regions of the monolith. Fig. 5b shows the gas phase volume fraction derived from 90 individual images; only the first image following a single excitation was considered in the analysis.

### 3.2. Two-phase flow in a trickle-bed reactor

The aim of this study is to compare liquid hold-up and wetting efficiency characteristics between the beds packed with 1.5 and 3 mm diameter alumina cylinders, and also to investigate the extent to which the dynamic liquid hold-up as a function of liquid superficial velocity is consistent with the percolation analysis of Crine et al. [1]. Good agreement with the aforementioned model is considered to be a validation of the MRI experimental and image analysis methodologies employed.

Fig. 6a and b show plots of dynamic liquid hold-up and wetting efficiency, respectively, against liquid superficial velocity for a constant gas velocity of 31.3 mm/s. Errors in the quoted values of hold-up and wetting efficiency are considered to be dominated by selection of the gating levels during data analysis. Therefore, the errors given are based on the variation in the respective parameters (i.e. $\chi_{\text{dynamic}}$ and $\chi_{\text{s}}$) introduced by selection of gating levels deviating by 10% from the reference gating level which is identified as the signal intensity just greater than the maximum noise level in the image. It is clearly seen from Fig. 6a that dynamic liquid hold-up increases more rapidly as a function of liquid superficial velocity within the 1.5 mm packing, and values of hold-up and wetting efficiency are always greater, for a given liquid velocity, for the 1.5 mm diameter packing relative to the 3 mm diameter packing. The line through the dynamic liquid hold-up data is the best fit of the percolation-based model described by Crine et al. [1]. The form of the expression for the dynamic liquid hold-up is:

$$\chi_{\text{dynamic}} = (KQ)^{1/3}\left(\frac{Q}{Q+Q_{\text{min}}}\right)^{2/3} \quad (1)$$

where $Q$ is the liquid superficial velocity and $Q_{\text{min}}$ is a minimum liquid superficial velocity. $K = k\mu_{\text{L}}a^2/\rho_{\text{L}}g$, where $k$ is a proportionality factor depending on the fluid and packing properties, $\mu_{\text{L}}$ the liquid dynamic viscosity, $\rho_{\text{L}}$ the liquid mass density, $a$ the specific surface of the packing, and $g$ is the acceler-

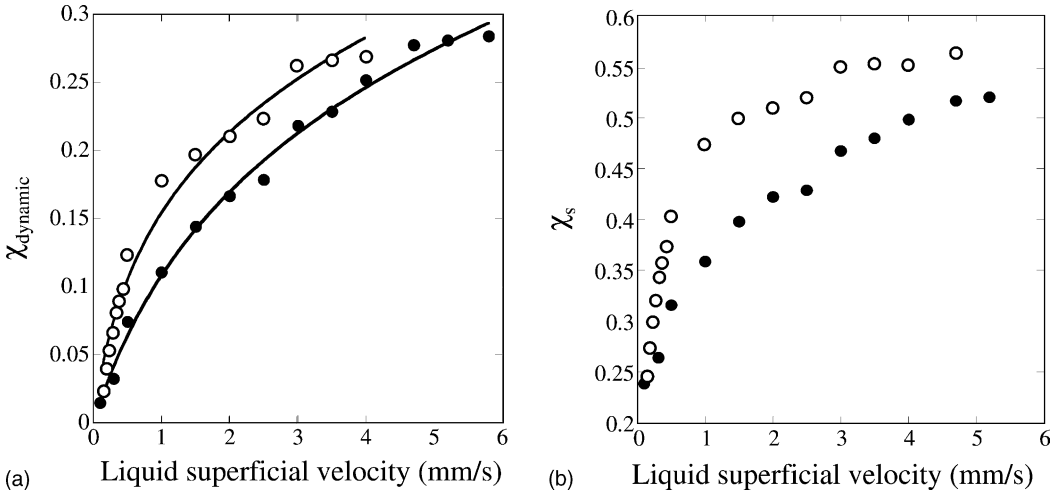


Fig. 6. Dynamic liquid hold-up and surface wetting data as a function of liquid superficial velocity for a constant gas flow velocity of 31.3 mm/s. Data are shown for both 1.5 mm (open circles) and 3 mm (filled circles) diameter extrudates. (a) Dynamic liquid hold-up; the typical standard deviation in the values quoted is ±0.01. The line shows the best fit of the percolation model, described in the text, to the data. (b) Surface wetting; the typical standard deviation in the values quoted is ±0.02. The values of surface wetting obtained are low compared to some earlier studies and this may be due to shortcomings in the experimental procedure in being able to identify thin liquid films on the surface of the packing elements.

ation due to gravity. Eq. (1) is fitted to the experimental data, with $Q_{min}$ and $K$ (i.e. $k$) as variables in the fit. As seen from Fig. 6a, the fit of Eq. (1) to the data is good. The values of $Q_{min}$ obtained are $3.56\times10^{-4}$ and $12.5\times10^{-4}$ m/s for the 1.5 and 3 mm diameter cylinders, respectively. Following the argument of Toye et al. [4], $Q_{min}$ characterises solid-phase (i.e. packing) wettability such that smaller values of $Q_{min}$ are associated with better packing wettability. This, as discussed earlier, is clearly supported by inspection of Fig. 6b. The values of $k$ obtained from the fitting procedure for the 1.5 and 3 mm diameter cylinders are 7.0 and 15.8, respectively.

## 4. Conclusions

MRI has been demonstrated to be able to provide a quantitative, dynamic visualisation of gas transport in bubble-train flow within a ceramic monolith, from which distributions of bubble size and bubble velocity within individual channels are obtained. For a monolith rated at 300 channels per square inch, increasing the gas flow rate from 100 through to 300 ml/min is shown not only to cause an increase in the number of larger gas bubbles within the monolith but also to produce a bimodal distribution of bubble velocities within the system. Bubbles moving counter-current to the direction of superficial flow are also observed. MRI visualisations of gas–liquid distribution during trickle flow within a fixed bed of commercial alumina catalyst support are presented. It is demonstrated that a quantitative determination of liquid hold-up and wetting efficiency can be determined using magnetic resonance techniques.

## Acknowledgements

We thank Johnson Matthey plc for provision of the ceramic monolith and cylindrical alumina packings. We also thank EPSRC, IMI and DTI LINK for financial support of this work.

## References

[1] M. Crine, P. Marchot, B. Lekhlif, G. L'Homme, Chem. Eng. Sci. 47 (1992) 2263.
[2] N. Reinecke, D. Mewes, Chem. Eng. Sci. 51 (1996) 2131.
[3] N.A. Tsochatzidis, A.J. Karabelas, Ind. Eng. Chem. Res. 33 (1994) 1299.

[4] D. Toye, P. Marchot, M. Crine, G. L'Homme, Meas. Sci. Technol. 7 (1996) 436.
[5] A.J. Sederman, M.L. Johns, P. Alexander, L.F. Gladden, Chem. Eng. Sci. 53 (1998) 2117.
[6] J. Park, S.J. Gibbs, AIChE J. 45 (1999) 655.
[7] M.L. Johns, A.J. Sederman, A.S. Bramley, P. Alexander, L.F. Gladden, AIChE J. 46 (2000) 2151.
[8] A.J. Sederman, L.F. Gladden, Chem. Eng. Sci. 56 (2001) 2615.
[9] M. Paterson-Beedle, K.P. Nott, L.E. Macaskie, L.D. Hall, Microb. Growth Biofilms 337 (2001) 285.
[10] U. Tallarek, E. Rapp, H. van As, E. Bayer, Angew. Chem. Int. Ed. 40 (2001) 1684.
[11] S.N.O. Williams, R.M. Callies, K.M. Brindle, Biotechnol. Bioeng. 56 (1997) 56.
[12] U. Tallarek, D. van Dusschoten, H. van As, E. Bayer, G. Guiochon, J. Phys. Chem. B 102 (1998) 3486.
[13] U. Tallarek, F.J. Vergeldt, H. van As, J. Phys. Chem. B 103 (1999) 7654.
[14] P.T. Callaghan, Principles of Nuclear Magnetic Resonance Micrsocopy, Clarendon Press, Oxford, 1991.
[15] L.F. Gladden, Chem. Eng. Sci. 49 (1994) 3339.
[16] T.A. Nijhuis, M.T. Kreutzer, A.C.J. Romijn, F. Kapteijn, J.A. Moulijn, Chem. Eng. Sci. 56 (2001) 823.
[17] I.V. Koptyug, S.A. Altobelli, E. Fukushima, A.V. Mateev, R.Z. Sagdeev, J. Magn. Reson. 147 (2000) 36.
[18] A.K. Heibel, T.W.J. Scheenen, J.J. Heiszwolf, H. van As, F. Kapteijn, J.A. Moulijn, Chem. Eng. Sci. 56 (2001) 5935.
[19] J. Hennig, A. Nauerth, H. Friedburg, Magn. Reson. Med. 3 (1986) 823.
[20] M.D. Mantle, A.J. Sederman, S. Raymahasay, E.H. Stitt, J.M. Winterbottom, L.F. Gladden, AIChE J. 48 (2002) 909.
[21] A.J. Sederman, M.D. Mantle, L.F. Gladden, J. Magn. Reson. 161 (2003) 76.